

REPORT DOCUMENTATION PAGE

Form Approved
OMB No. 0704-0188

Public reporting burden for this collection of information is estimated to average 1 hour per response, including the time for reviewing instructions, searching existing data sources, gathering and maintaining the data needed, and completing and reviewing this collection of information. Send comments regarding this burden estimate or any other aspect of this collection of information, including suggestions for reducing this burden to Department of Defense, Washington Headquarters Services, Directorate for Information Operations and Reports (0704-0188), 1215 Jefferson Davis Highway, Suite 1204, Arlington, VA 22202-4302. Respondents should be aware that notwithstanding any other provision of law, no person shall be subject to any penalty for failing to comply with a collection of information if it does not display a currently valid OMB control number. PLEASE DO NOT RETURN YOUR FORM TO THE ABOVE ADDRESS.

1. REPORT DATE (DD-MM-YYYY) 07-24-2006		2. REPORT TYPE Final Report		3. DATES COVERED (From - To) 03/01/2003 to 12/31/2005	
4. TITLE AND SUBTITLE Discrete Element Method for Modeling Penetration				5a. CONTRACT NUMBER	
				5b. GRANT NUMBER F49620-03-1-0216	
				5c. PROGRAM ELEMENT NUMBER	
6. AUTHOR(S) Michael E. Plesha				5d. PROJECT NUMBER	
				5e. TASK NUMBER	
				5f. WORK UNIT NUMBER	
7. PERFORMING ORGANIZATION NAME(S) AND ADDRESS(ES) University of Wisconsin Dept. of Engineering Physics 1500 Engineering Drive Madison, WI 53706				8. PERFORMING ORGANIZATION REPORT NUMBER	
9. SPONSORING / MONITORING AGENCY NAME(S) AND ADDRESS(ES) AFOSR/NM 875 N. Randolph St, Ste 325 Arlington VA 22203 Dr Fahro				10. SPONSOR/MONITOR'S ACRONYM(S) 1. AFRL-SR-AR-TR-06-0276	
12. DISTRIBUTION / AVAILABILITY STATEMENT Unclassified - Unlimmited distribution.					
Approved for public release, distribution unlimited					
13. SUPPLEMENTARY NOTES					
14. ABSTRACT This research resulted in the development of the Discrete Element Method (DEM) as a general, robust, and scalable computer technique for unified modeling of the mechanical behavior of solid and particulate materials, including the transition from solid phase to particulate phase. Applications include gross damage of structures due to extreme load events, and high speed penetration of structures, involving materials such as concrete, rock, and novel combinations of these. This computer approach is useful for assessing vulnerability of military and civilian facilities such as nuclear power reactors, transportation facilities, buildings, and so on, and for assessing efficacy of military operations involving such structures. One of the primary accomplishments of this research is the development of interelement potentials for the DEM method such that accurate and convergent results are obtained.					
15. SUBJECT TERMS Discrete element method, DEM, damage, penetration.					
16. SECURITY CLASSIFICATION OF:			17. LIMITATION OF ABSTRACT	18. NUMBER OF PAGES	19a. NAME OF RESPONSIBLE PERSON
a. REPORT Unclassified	b. ABSTRACT Unclassified	c. THIS PAGE Unclassified			Michael E. Plesha
				35	19b. TELEPHONE NUMBER (include area code) 608-262-5741

Final Report: Discrete Element Method for Modeling Penetration

AFOSR Grant No. F49620-03-1-0216
Project Period: 03/01/2003 to 12/31/2005

Michael E. Plesha

Department of Engineering Physics, University of Wisconsin, Madison, Wisconsin 53706
plesha@engr.wisc.edu

Personnel Supported:

people: Federico A. Tavarez, graduate student
Can Bora, graduate student
Michael E. Plesha, P.I.
organizations: None
collaborators: None

Abstract

This research resulted in the development of the Discrete Element Method (DEM) as a general, robust, and scalable computer technique for unified modeling of the mechanical behavior of solid and particulate materials, including the transition from solid phase to particulate phase. Applications include gross damage of structures due to extreme load events, and high speed penetration of structures, involving materials such as concrete, rock, and novel combinations of these. This computer approach is useful for assessing vulnerability of military and civilian facilities such as nuclear power reactors, transportation facilities, buildings, and so on, and for assessing efficacy of military operations involving such structures. One of the primary accomplishments of this research is the development of interelement potentials for the DEM method such that accurate and convergent results are obtained.

1. Executive Summary

Although empirical equations for local damage give a reasonable prediction of quantities such as depth of penetration, they do not describe the behavior of the concrete structure. In order to improve the understanding of concrete subjected to severe loading, a combination of experiments and numerical methods are needed for a complete analysis of the structural behavior where the material fracture mechanisms can be studied in detail. In this work, a discrete element method was developed as a general computer technique for unified modeling of the mechanical behavior of solid and particulate materials,

including the transition from solid phase to particulate phase. As a result of this research, the following contributions in the field of computer modeling by the discrete element method were made:

- A theoretical method was developed to determine DEM contact normal and tangential stiffnesses as functions of known material properties so that convergence is obtained and the correct elastic behavior is produced, depending on the arrangement of the DEM elements in the discretization. For a simple cubic assembly, the normal and tangential stiffnesses are

$$K_n = K_t = E^*t \quad (1.1)$$

For a close-packed assembly and for an irregular assembly, the normal and tangential stiffnesses are

$$K_n = \frac{1}{\sqrt{3}(1-\nu^*)} E^*t \quad (1.2)$$

$$K_t = \frac{(1-3\nu^*)}{(1+\nu^*)} K_n = \frac{(1-3\nu^*)}{\sqrt{3}(1-\nu^{*2})} E^*t \quad (1.3)$$

where E^* and ν^* are defined for plane stress and plane strain situations in terms of elastic modulus E , Poisson's ratio ν , and thickness t by

	<u>plane stress</u>	<u>plane strain</u>	
$E^* =$	E	$\frac{E}{(1-\nu^2)}$	(1.4)

$\nu^* =$	ν	$\frac{\nu}{(1-\nu)}$	(1.5)
-----------	-------	-----------------------	-------

- Regarding contact failure for close-packed and irregular DEM assemblies, a novel DEM contact behavior was developed in order to account for different failure modes. That is, when failure is dictated by the material's fracture toughness K_{Ic} or the material's ultimate tensile strength σ_{ult} . The contact stress-displacement curve, shown in Figure 1.1, is proposed to be linear until the contact normal and shear stresses reach critical values given by

$$\sigma_n^{crit} = \frac{f_n^{crit}}{2Rt} \quad \text{where} \quad f_n^{crit} = \frac{(Rt)\sigma_{ult}}{2(1-\nu^*)} \left(\sqrt{3} - \frac{\nu^*}{\sqrt{3}} \right) \quad (1.6)$$

$$\sigma_t^{crit} = \frac{f_t^{crit}}{2Rt} \quad \text{where} \quad f_t^{crit} = \frac{(Rt)\sigma_{ult}}{2(1-\nu^*)} (1-3\nu^*) \quad (1.7)$$

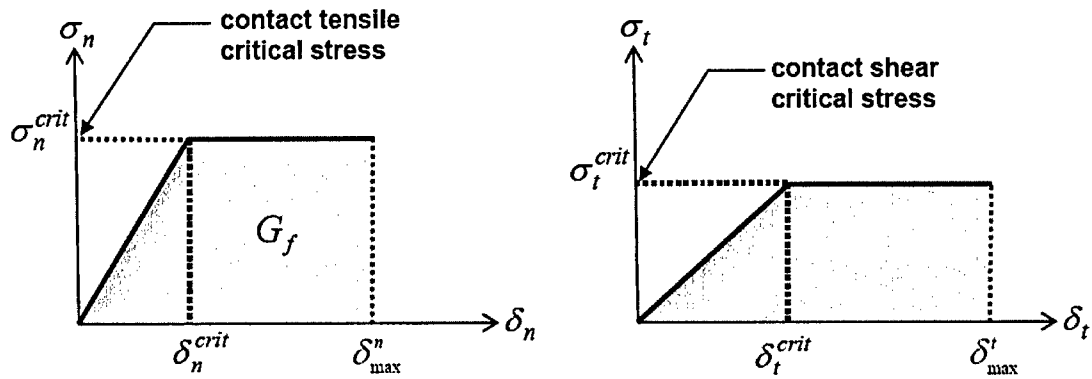


Figure 1.1 DEM inter-element constitutive behavior.

After the contact forces reach the values given by Equations 1.6 and 1.7, the contact behavior is proposed to be plastic until the area under the stress-displacement curve for the normal direction spring reaches the material's fracture energy, given by

$$G_f = \frac{K_{lc}^2}{E^*} \quad (1.8)$$

The maximum normal displacement is then given by

$$\delta_{max}^n = \frac{K_{lc}^2}{\sigma_n^{crit} E^*} + \frac{\delta_n^{crit}}{2} \quad \text{where} \quad \delta_n^{crit} = \frac{f_n^{crit}}{K_n} \quad (1.9)$$

- For purposes of selecting a time step size for integrating the equations of motion, a new method was developed to accurately bound the maximum frequency of vibration in a DEM model, which gives a more accurate prediction than the ad hoc approximation that is usually implemented.
- The proposed DEM method was used to model penetration events on concrete targets. To increase the accuracy of numerical analyses for projectile impact, nonlinear compression behavior and strain rate effects were incorporated into the model. Penetration depth, scabbing velocity, and ballistic limit values were obtained and compared with available empirical formulae obtained from the literature and a reasonable agreement was found.

The major findings are summarized below.

Convergence Studies

The proposed method used a DEM model of a unit cell of homogeneous material to theoretically develop criteria for contact stiffness and failure so that convergence of elastic response and damage response due crack growth is established for the representative models considered in the study. The simulations showed very good correlation (for both the elastic behavior and fracture) with theoretical results. However, the convergence rate was not clear from the simulations performed, and it appears to change depending on element arrangement (i.e. simple cubic, close-packed, or irregular).

Nevertheless, the use of theory to determine contact parameters was very beneficial because it avoided the tedious procedure of model calibration for a given mesh refinement.

Megaclustering and Fracture

The technique used for solid model development (megaclustering) proved to be an effective method of introducing irregularity in the model, with no preferential directions for fracture. The technique allowed for the mesh to have areas of stress concentration where crack propagation would be more likely to occur. For the type of element arrangement produced by megaclustering, the energy-based criterion (influenced by strain rate effects) developed for contact failure proved to be more appropriate than a criterion based purely in the material's ultimate tensile strength or fracture toughness.

Penetration Simulations

The numerical results obtained in this work showed that DEM is a very useful tool for simulating impact problems and projectile penetration into concrete structures. Due to the strain rates produced by such events, material properties such as tensile strength, compressive strength, and fracture energy increased considerably. Results for penetration depth, scabbing velocity, and ballistic limit were in agreement with the bounds given by the available empirical formulae, especially the BRL equations to predict scabbing velocity and ballistic limit. However, due to the parameters chosen for the model, global deformation and flexural cracking occurred in the models, which influenced the level of damage in the target.

Contact Compression Behavior

The incorporation of nonlinear compression behavior to account for material "densification" due to concrete compaction proved to have a considerable influence on the structural response of a concrete target subjected to a projectile penetration. The addition of this behavior allowed the medium to absorb energy in the material immediately ahead of the projectile, allowing the numerical results to correlate better with the empirical formulae. However, the implementation of this behavior increased the ductility of the medium, influencing the amount of spalling at the front face and scabbing at the back face of the target.

Detailed Summary of Work

2. Overview of the Discrete Element Method (DEM)

The discrete element method (DEM) discretizes a material using rigid elements of simple shape that interact with neighboring elements according to interaction laws that are applied at points of contact. The rigid elements are typically of circular or spherical shape due to the simplicity and speed of the contact detection algorithm. However, several researchers have applied the method using elements of polygonal shape (Heuze et al. 1993; Kun and Herrmann 1996; Bolander and Saito 1997; Camborde et al. 2000; Prochazka 2004).

The method is ideal for modeling many problems not accessible to traditional continuum-based methods such as finite differences and finite elements since it has the advantage of inherently capturing large deformations and solid phase changes which are commonly found in granular media. Other applications involving material separation and progressive failure phenomena include concrete structural failure, rock blasting operations, and fracture of ceramic or other quasibrittle materials under high velocity impact. In contrast to finite elements, the method is particularly attractive for modeling geomaterials due to its ability construct a mesh that is not completely continuous and homogeneous, as shown in Figure 2.1. Since the mesh is constructed by rigid elements that interact with each other at points of contact, the DEM mesh has the capability of easily constructing a medium with voids, imperfections and heterogeneities, as shown in Figure 2.1(b), which are present in rock, concrete, asphalt, and other geomaterials.

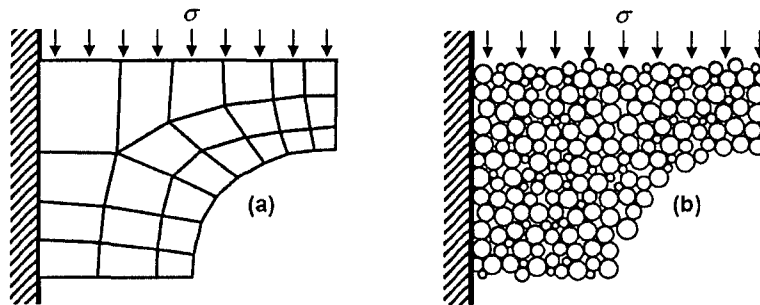


Figure 2.1 Finite element mesh (a) vs. discrete element mesh (b).

The analysis algorithm consists of three major computational steps: *contact processing*, in which contact forces are calculated, *element motion*, in which element displacements are computed, and *contact detection*, in which new contacts are identified and broken contacts are removed. In a DEM analysis, the interaction of the elements is treated as a dynamic process that alternates between the application of Newton's second law and the evaluation of a force-displacement law at the contacts. Newton's second law gives the acceleration of an element resulting from the forces acting on it, including gravitational forces, external forces prescribed by boundary conditions, and internal forces developed at interparticle contacts. The acceleration is then integrated to obtain the velocity and

displacement. The force-displacement law is used to find contact forces from known displacements. This process is described in the following sections.

Element Interaction Models

When modeling a solid with no initial cracks (i.e., a nominally homogeneous material), all contacts in the assembled medium are initially bonded with the behavior that is schematically illustrated in Figure 2.2. During the course of a simulation, if a bonded contact fails, according to criteria to be described, the contact becomes frictional as shown also in Figure 2.2, if indeed the contact still exists (i.e., if the two DEM elements are still being pressed into one another), or the contact is destroyed if the two elements are separating. The computer implementation uses *Rayleigh* or *proportional* damping (Cook et al. 1989), and therefore damping parameters are chosen as fractions of critical damping at two desired frequencies.

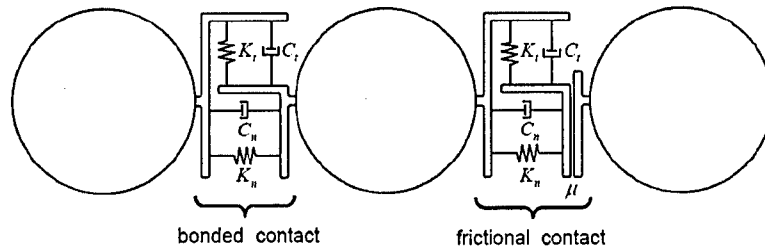


Figure 2.2 Discrete element interaction models for bonded and frictional contacts.

Bonded Contact

In the bonded contact, the normal spring acts in tension and compression, having a linear elastic behavior between force and displacement, as shown in Figure 2.3(a). The shear spring also has a linear elastic behavior, shown in Figure 2.3(b), with an elastic constant that is usually lower than that of the normal spring.

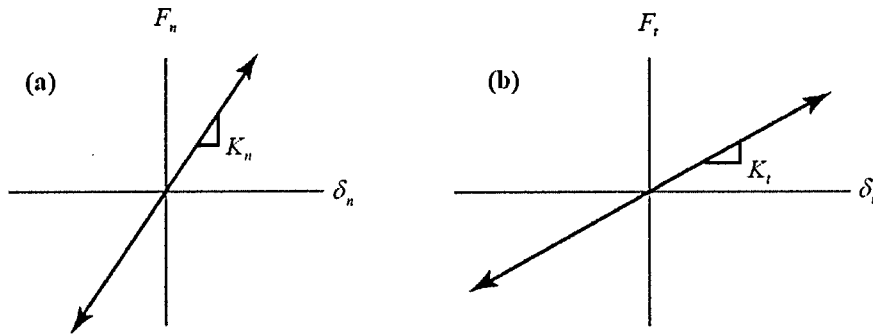


Figure 2.3 Constitutive relation for bonded contact.

Frictional Contact

The normal-direction spring in the frictional contact shown in Figure 2.4(a) acts only in compression. In the tangential direction, shown in Figure 2.4(b), the shear force is monitored against a maximum possible value according to a Coulomb-type friction law. The maximum shear force is defined as

$$|F_t^{\max}| = -\mu F_n + c \quad (2.1)$$

where μ and c are the friction coefficient and the cohesion between the elements, respectively. If the computed shear force F_t is larger than F_t^{\max} , F_t is set to F_t^{\max} , allowing the elements to slide.

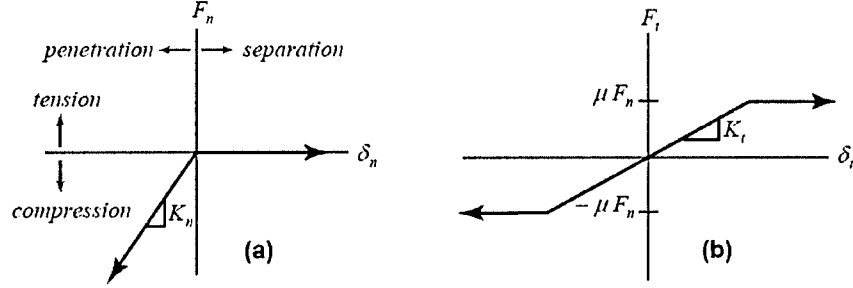


Figure 2.4 Constitutive relation for frictional contact.

Equations of Motion

After computing all the forces acting on an element, the displacement, velocities and accelerations of each element are computed using the central difference method, where details are given in Tavarez (2005) and Tavarez and Plesha (2006). Since explicit integration is conditionally stable, the time step Δt must satisfy

$$\Delta t < \frac{2}{\omega_{\max}} \left(\sqrt{1 - \xi^2} - \xi \right) \quad (2.2)$$

for linear viscous damping, where ξ is the fraction of critical damping at ω_{\max} , which is the highest natural frequency of the mesh. For practical problems, ω_{\max} is rarely known because it is expensive to determine. Therefore, an accurate upper bound for this frequency is desirable.

Frequency Bound

In this work, we have developed a new approach for obtaining an upper bound for ω_{\max} by computing the largest eigenvalue for a unit cell of DEM elements as shown in Figure 2.5. This unit cell consists of seven rigid elements arranged in a close-packed assembly. A complete mesh for a structure is then constructed by discretizing the medium using a large number of these DEM unit cells inter-connected with one another. Therefore, $(\omega_{\max})_e$ can now be obtained by calculating the largest eigenvalue of the DEM unit cell structure. As will be shown in Section 3, the construction and analysis of this DEM unit cell was also necessary to obtain the correct values for contact stiffness for modeling elastic material behavior.

Mass and stiffness matrices were computed for the DEM unit cell shown in Figure 2.5, which consists of 21 degrees of freedom (14 translational d.o.f. and 7 rotational d.o.f.). Values for the stiffness and mass matrices are given in Appendix A of Tavarez (2005). Frequency analysis of the unit cell shown in Figure 2.5 provides $(\omega_{\max})_e \approx 3.742 \sqrt{K_n/m}$, where m is the mass of each DEM element and K_n is the normal

contact stiffness. Substituting this frequency into Equation 2.2, we obtain an accurate upper bound estimate for the critical time step Δt_{crit} as

$$\Delta t_{crit} \approx 0.535 \sqrt{m/K_n} \left(\sqrt{1 - \xi^2} - \xi \right) \quad (2.3)$$

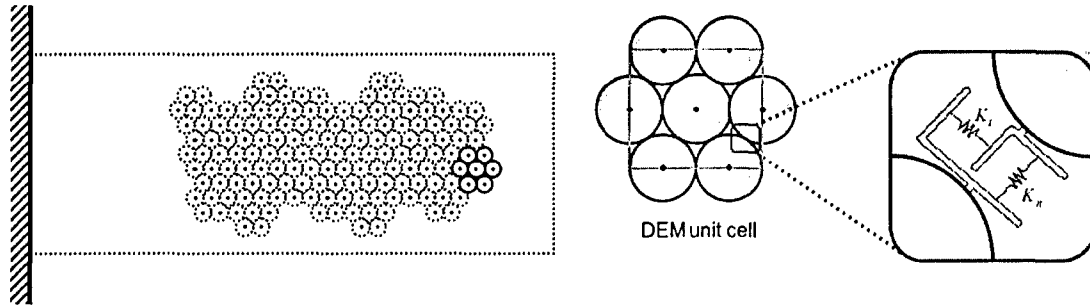


Figure 2.5. DEM discretization and unit cell used for computing maximum element frequency.

3. DEM for modeling brittle materials

We use the concept of *clusters* to represent solid media. Clusters are formed by bonding a number of circular-shaped DEM elements into a semi-rigid configuration. To model a solid such as concrete, this concept can be extended to *megaclustering* wherein the entire volume of a solid is modeled by bonding individual clusters together. Once the model's geometry is established, boundary conditions are prescribed. This generation scheme will allow for "molding" of structures or structural components of arbitrary shape.

Determination of Inter-Element Normal and Shear Stiffness

The macroscopic linear elastic behavior of isotropic materials can be characterized by two elastic constants: Young's modulus E and Poisson's ratio ν , and the physical parameters governing DEM element interactions have typically been determined by the ad hoc process of validating a numerical simulation of a standard laboratory test with an actual experimental result (Potyondy et al. 1996; Magnier and Donze 1998). Unfortunately, if a new discretization for a particular problem is produced but with different DEM element size (such as making element size smaller to improve accuracy of the simulation), the calibration process would need to be repeated in its entirety to obtain the new DEM parameters.

In our study we developed a new approach wherein we theoretically established the interelement normal and tangential stiffnesses (and failure parameters, to be discussed later) as functions of element size and commonly accepted elastic constants including Young's modulus and Poisson's ratio. This was done by the analysis of a DEM unit cell of material. Figure 3.1(a) shows an isotropic solid material element (with known elastic modulus and Poisson's ratio) subjected to uniaxial stress. The volume of material is then modeled using the DEM unit cell shown in Figure 3.1(b). Using this unit cell, the normal

and tangential spring constants can then be determined as functions of the known elastic modulus and Poisson's ratio of the material, and if needed the DEM element size.

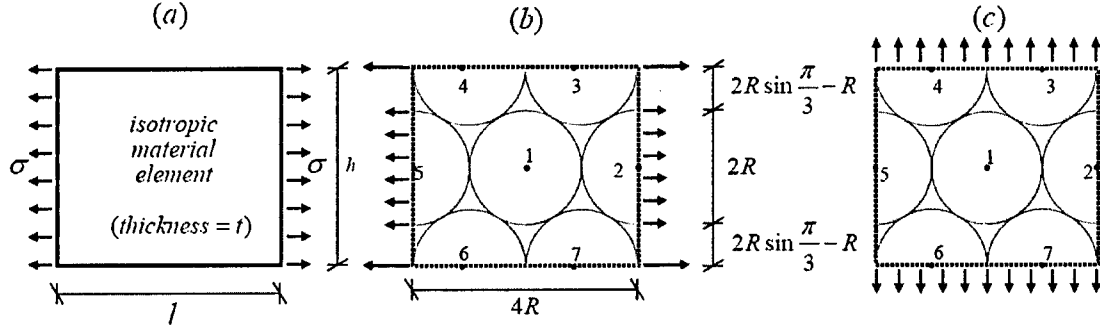


Figure 3.1 DEM unit cell for determination of inter-element spring constants.

The unit cell in Figure 3.1(b) contains 7 elements having 3 degrees of freedom per element (two translations and one rotation). By requiring the deformation of this unit cell to agree with the exact response for an isotropic material (see Tavarez 2005), we obtain the normal and tangential stiffnesses to be

$$K_n = \frac{1}{\sqrt{3}(1-\nu^*)} E^* t \quad (3.1)$$

$$K_t = \left(\frac{1-3\nu^*}{1+\nu^*} \right) K_n = \frac{(1-3\nu^*)}{\sqrt{3}(1-\nu^{*2})} E^* t \quad (3.2)$$

where E^* and ν^* are defined for plane stress and plane strain situations by

$$E^* = \begin{matrix} \text{plane stress} & \text{plane strain} \\ E & \frac{E}{(1-\nu^2)} \end{matrix} \quad (3.2)$$

$$\nu^* = \begin{matrix} \text{plane stress} & \text{plane strain} \\ \nu & \frac{\nu}{(1-\nu)} \end{matrix} \quad (3.4)$$

DEM Fracture Criteria

Different approaches have been used in the past to model fracture in DEM, where most of this work considers a tensile force limit for contact failure (Zubelewicz and Bazant 1987; Masuya et al. 1994; Bolander and Saito 1997; Brara et al. 2001; Mishra and Thornton 2001). That is, if the tensile force in a certain contact exceeds a limit value, the contact breaks and can no longer support tensile forces. This force limit is usually determined by calibrating DEM simulation results to available experimental data from tensile and compressive tests performed on a particular material. However, since force transmission through a DEM medium can only occur via the inter-element contacts, the number of contacts within a DEM medium will most likely affect the fracture behavior. Therefore, this contact force limit is most likely to be element size dependent. Taking into account this element size dependency, several researchers have considered a failure

criterion based on the tensile strength of the material, using a DEM model consisting of two elements, as shown in Figure 3.2 (Sawamoto et al. 1998). The maximum normal stress failure criterion states that failure occurs when the maximum principal stress reaches the tensile strength of the material. The tensile force required to break the contact is then determined by

$$f_{ult} = \sigma_{ult} (2R)t \quad (3.5)$$

where σ_{ult} is the tensile strength of the material. As seen in Equation 3.5, this criterion suggests that the tensile force required for contact failure is linearly proportional to the DEM element radius R .

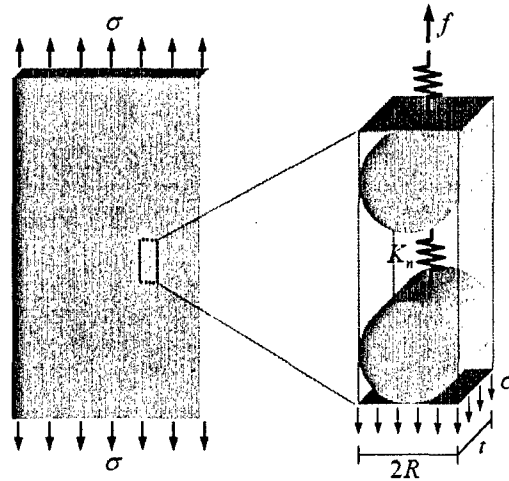


Figure 3.2 Tensile strength criterion for fracture.

Several researchers have imposed a limit in both the tensile and shear stress in the contact, as shown in Figure 3.3 (Potyondy et al. 1996; Donze et al. 1997; Magnier and Donze 1998). These thresholds are also selected according to shear and tensile strengths determined in laboratory experiments.

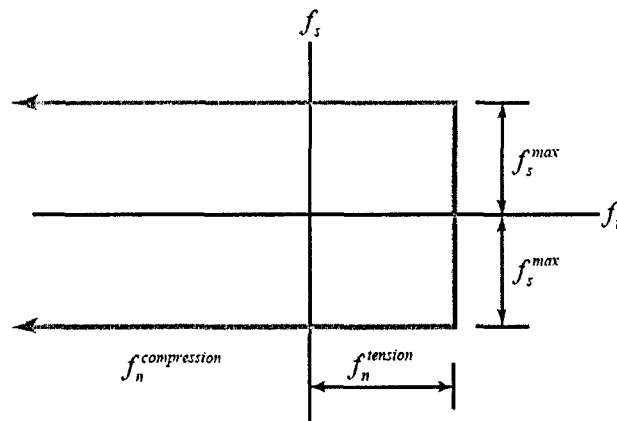


Figure 3.3 Failure surface for bonded contact considering tensile and shear limits.

Fracture Toughness Failure Criterion

In what follows, we theoretically develop a contact failure criterion based on DEM element size and known material properties. Since this method will eventually be used to model extensive cracking and fragmentation in a medium, a criterion based only on the ultimate tensile strength of the material would produce inaccurate results when stress singularities arise due to flaws and cracking in the medium. The following approach addresses this issue.

The results to be described here begin with the original work of Potyondy and Cundall (2004). In their work, they postulate a breaking strength between the bonds of contacting DEM elements, and then address the issue of determining the fracture toughness of the material that is being modeled by the DEM discretization. The approach described herein differs from theirs in that we view the fracture toughness as a fundamental material parameter, and then attempt to use theory to develop expressions for the behavior of bonds between contacting DEM elements. A main feature of such an approach is that it promises to provide *convergence*. That is, it provides a precise specification of how the contact behavior between DEM elements must change as a function of element size so that convergence to the exact solution is achieved as the DEM element size becomes smaller during model refinement. To model the progressive failure of a solid due to crack growth, a local rupture criterion is applied to the bonded contacts between interacting elements. The plane stress/strain near crack tip stress field for pure Mode I loading in a homogeneous, isotropic, linear elastic material is given by (Anderson 1994):

$$\sigma_{ij}(r, \theta) = \frac{K_I}{\sqrt{2\pi r}} F_{ij}(\theta) + \sum_{n=0}^{\infty} A_n r^{n/2} F_{ij}^{(n)}(\theta) \quad (3.6)$$

Since crack growth is controlled by the stresses near the crack tip, i.e., at small r , the first term in Equation 3.6 gives the highest contribution to the stress field at the crack tip. Therefore, keeping only the first term in Equation 3.6, the well known expression for the stresses close to the crack tip, shown in Figure 3.4, is obtained.

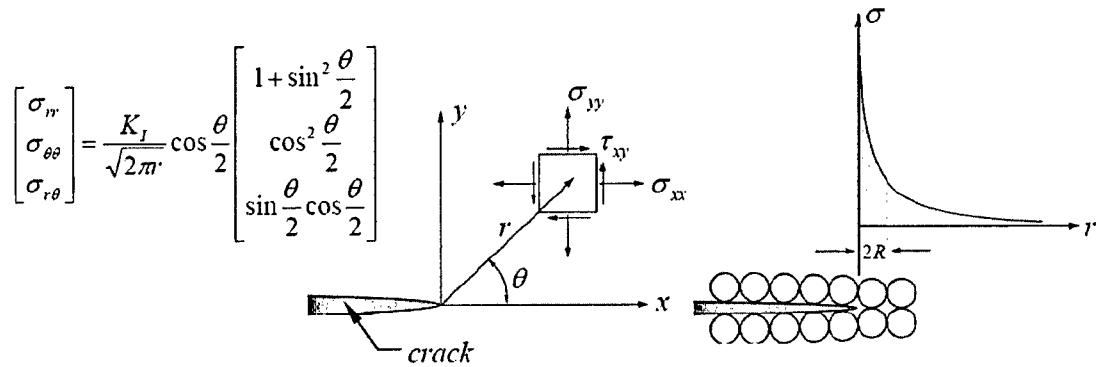


Figure 3.4 Crack tip stress field for pure Mode I cracking.

Restricting attention to $\theta = 0$, the stress $\sigma_{\theta\theta}$ is then

$$\sigma_{\theta\theta} = \frac{K_I}{\sqrt{2\pi r}} \quad (3.7)$$

The force required to advance the crack by breaking the contact at the crack tip of a DEM model is determined by integrating the stress field over the DEM element diameter and thickness (Potyondy and Cundall 2004), as shown in Figure 3.4. Therefore,

$$f = \int_0^{2R} \int_0^t \sigma_{\theta\theta} dr dt = \int_0^{2R} \int_0^t \frac{K_I}{\sqrt{2\pi}} tr^{-1/2} dr dt \quad (3.8)$$

$$f = 2K_I t \sqrt{\frac{R}{\pi}} \quad (3.9)$$

where f is defined in Figure 3.2. According to Irwin's criterion, cracking will occur when the value of K_I reaches the material's fracture toughness K_{Ic} . Therefore, the required force to break the contact is given by

$$f_{ult} = 2K_{Ic} t \sqrt{\frac{R}{\pi}} \quad (3.10)$$

As shown in Equation 3.10, material failure parameters in this approach are dependent on DEM element size and the fracture toughness of the material. As described above, this result is very significant because it prescribes exactly how the DEM interelement strength must change as a function of element size so that convergence is obtained as element radius R vanishes in the limit of mesh refinement.

4. Convergence of DEM simulations

Before discussing convergence of DEM simulations, it is instructive to briefly discuss convergence of simulations performed using the finite element method (FEM). In a typical FEM simulation, a problem is discretized using a user-selected number of degrees of freedom. If the problem being modeled is elliptic (linear-elastic, small deformations, no singularities such as point forces or cracks, etc.) then it is expected that accuracy of results will improve as the model is refined by adding more degrees of freedom, and that convergence to the exact solution will be obtained in the limit that an infinite number of degrees of freedom are used. Fortunately and very importantly, there are theoretical results showing that FEM simulations indeed do converge, and furthermore the rate of convergence for most popular element types is known. In this study we attempt to help establish similar results for DEM simulations.

We have studied, and established the convergence properties for DEM models for applications to axial deformation of a bar, including the Poisson effect, and bending deformation of a beam, for simple cubic arrangements of DEM elements, close packed arrangements, and irregular (random) arrangements. In all cases, the interelement potentials we have described in Section 3 give convergence as the number of DEM element used in the discretization is increased. In this section, we present results for just one of these studies, namely bending deformations using a simple cubic arrangement of DEM elements.

Convergence for Elastic Response of a Cantilever Beam

A DEM model of a cantilever beam subjected to a sinusoidal tip load with frequency ω was considered. A closed-form solution for this problem can be obtained by

idealizing the structure as a single degree of freedom (SDOF) model with natural frequency equal to the fundamental natural frequency of a continuous cantilever beam (i.e., $\omega_n = 3.52\sqrt{EI/ML^3}$). However, this solution assumes that only the fundamental mode shape of the cantilever beam is excited by the loading conditions. Since higher modes might not be insignificant for the degree of precision needed, the accuracy of the DEM simulations for this problem will be studied by also comparing the DEM results with simulations performed using finite element analysis (FEA). The finite element analysis was performed in ANSYS, where the cantilever beam was discretized using 1440 four-node plane quadrilateral elements.

Figure 4.1 shows three DEM discretizations for the cantilever beam using close-packed assemblies with 81, 729, and 6561 elements, respectively. The element size was reduced by a factor of 3 for each refinement. All DEM simulations use the values for normal and tangential spring stiffness given by Equations 3.1 and 3.2 with $E = 1.2$ GPa and $\nu = 0.3$. The forcing frequency was chosen to be 0.2 times the value of the fundamental natural frequency, and a fraction of critical damping of $\xi = 10\%$ was used at this frequency. Figure 4.2(a) shows the tip displacement as a function of time for the three models. Figure 4.2(b) shows the tip displacement obtained by the finest mesh along with the SDOF solution and the FEA solution.

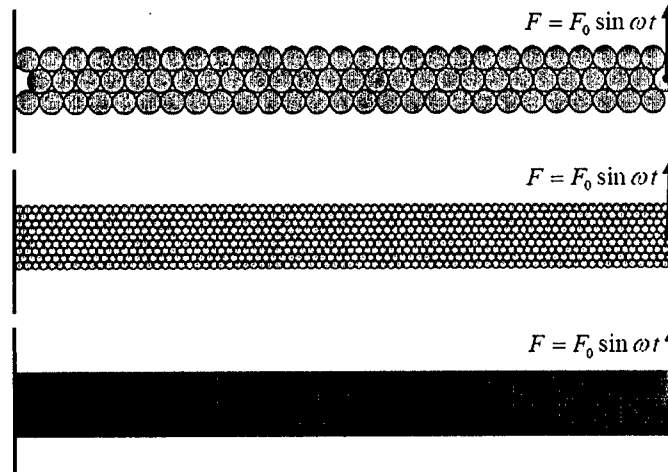


Figure 4.1 DEM models of cantilever beam using a close-packed assembly.

As shown in Figure 4.2(b), there is also excellent agreement between the DEM solution and both the SDOF solution and the FEA solution, and results also appear to converge to a definite value in the limit of mesh refinement. However, since the ratio ω/ω_n was chosen to be greater for these models ($\omega/\omega_n = 0.2$), the importance of the higher modes of vibration, which are neglected in the SDOF model, is greater and thus, the DEM solution agrees slightly better with the finite element solution. Applying Richardson extrapolation (Cook, et al 1989) to the results of these three DEM models provides an estimate of $\delta_{max} = 0.4754$ m as the steady state maximum amplitude of vibration that the DEM models will converge to. The finite element solution provides $\delta_{FEM} = 0.4749$ m which is within 0.1 % of the DEM extrapolated solution.

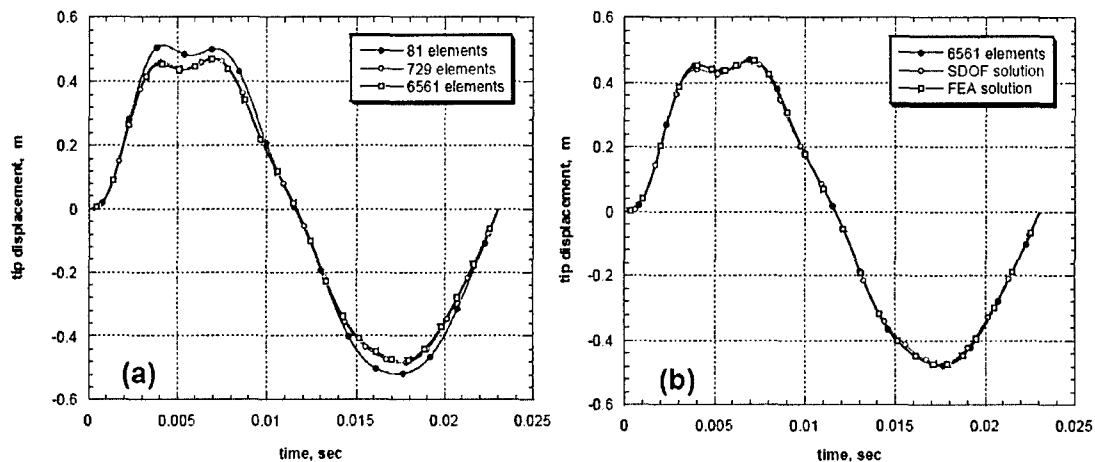


Figure 4.2 DEM tip displacement results and comparison with theoretical solution using a close-packed assembly.

We also conducted convergence analyses for irregular (random) DEM discretizations. While these results appear to show convergence, it is interesting to note that contrary to the cases using simple cubic and close-packed arrays, the irregularly structured models seem to become more flexible as the mesh is refined. Moreover, results appear to converge to a solution that is lower (about 6.5%) than the FEA solution. Therefore, it is concluded that when Equations 3.1 and 3.2 are used for an irregular DEM assembly, results may underpredict the steady state response of the beam. One possible explanation for why the models become stiffer as the DEM mesh is refined (for the simple cubic and close-packed arrangements) could be that for each refinement, there are contact springs that are closer to the top and bottom surfaces of the beam, increasing the flexural stiffness of the model. This appears to have a greater effect on the behavior of the model than adding more degrees of freedom, which usually results in making a model more flexible. On the other hand, the addition of degrees of freedom appears to have a greater effect on the behavior of the model when using an irregular arrangement, resulting in a numerical solution that becomes “softer” as the mesh is refined.

Rate of Convergence

The purpose of having at least three different results for each element arrangement pattern was to determine the rate of convergence for the DEM analysis. Using the results of three meshes, the rate of convergence (if uniform) can be computed using Richardson extrapolation (Cook et al. 1989) as

$$p = \log \left(\frac{\phi_1 - \phi_2}{\phi_2 - \phi_3} \right) \frac{1}{\log \alpha} \quad (4.1)$$

where ϕ_i are, in this case, the values for the maximum steady state displacement for the three different discretizations, and α is the element size reduction factor for each mesh refinement, which must be a constant for each refinement. Table 4.1 shows the rate convergence computed for the three different meshes used for representing the cantilever beam.

Table 4.1 Summary of convergence results for the three model lattices used.

DEM Element Arrangement	Number of Particles Used			α	p
	Mesh 1	Mesh 2	Mesh 3		
simple cubic	90	810	7290	3	4.57
close-packed	81	729	6561	3	1.52
irregular	600	1200	2400	$\sqrt{2}$	3.00

Unfortunately, the rate of convergence was different for each element arrangement pattern. As shown in this table, the simple cubic element arrangement pattern showed the largest rate of convergence with a value of $p = 4.57$. However, this surprisingly large value is no doubt not accurate and might be due to the fact that the use of only 90 elements in a simple cubic discretization is too coarse of a mesh for this problem to provide a uniform rate of convergence. Consequently, the result of mesh 1 is considerably lower than the results of meshes 2 and 3, yielding an apparent large rate of convergence. The same argument can be conjectured for the rate of convergence computed for the irregular discretization. On the other hand, the rate of convergence for the close-packed discretization was $p = 1.52$, which is a more reasonable value. However, while these results are the first of their kind that we are aware of, considerable additional work is still required to adequately understand the convergence properties of DEM simulations of elastic response in solids.

Convergence for Damage Response due to Crack Growth

In order to study convergence when the response includes damage, three DEM models representing a plate with a crack subjected to pure Mode I loading were developed. The material modeled by these DEM meshes has Young's modulus $E = 29.7$ GPa, Poisson's ratio $\nu = 0.3$, and fracture toughness $K_{Ic} = 1.0$ MPa \sqrt{m} . The models, shown in Figure 4.3, consist of 256, 1024, and 4096 elements, respectively. As such, the DEM element radius was reduced by a factor of 2 with each mesh refinement. The edge crack (shown by the solid line at the center of each model), was created by giving contacts along the crack the standard behavior described by the frictional contact mechanism shown in Figure 2.4. That is, if two initially contacting DEM elements on the crack surface are separated (which is the case for all of the simulations of the models in Figure 4.3), there are no forces acting between them, while if they remain in contact, they have Coulomb friction response.

As seen in Figure 4.3, these models were constructed using a simple cubic assembly of elements. This type of assembly was chosen due to its simplicity for theoretical analysis leading to Equation 3.10. Even though symmetry could have been used for this type of problem to reduce the number of elements, it was decided to model the entire problem in order to avoid the application of symmetry constraints to each of the DEM elements located at the symmetry boundary. For the loading shown in Figure 4.3, the displacements are such that the crack surface undergoes zero vertical displacement, while the upper boundary moves in the upward direction and the lower boundary moves

an equal amount in the downward direction. With a simple cubic assembly, the crack plane is perpendicular to the direction of the far field stress and thus the force at the crack tip is carried by only the normal direction springs ahead of the crack tip. For these models, the normal and tangential stiffnesses were assumed to be

$$K_n = K_t = Et \quad (4.2)$$

The results of the DEM simulations are shown in Figure 4.3, where the solid data points represent values of the displacement and far field stress that cause the crack to propagate unstably across the model. Very importantly, these results appear to converge and an extrapolated value for the far field stress that causes unstable crack growth can be computed. Applying Richardson extrapolation to the results of these three models provides an estimate of $\sigma_{crit} = 2.78$ MPa as the value of the far field stress that the DEM models will converge to.

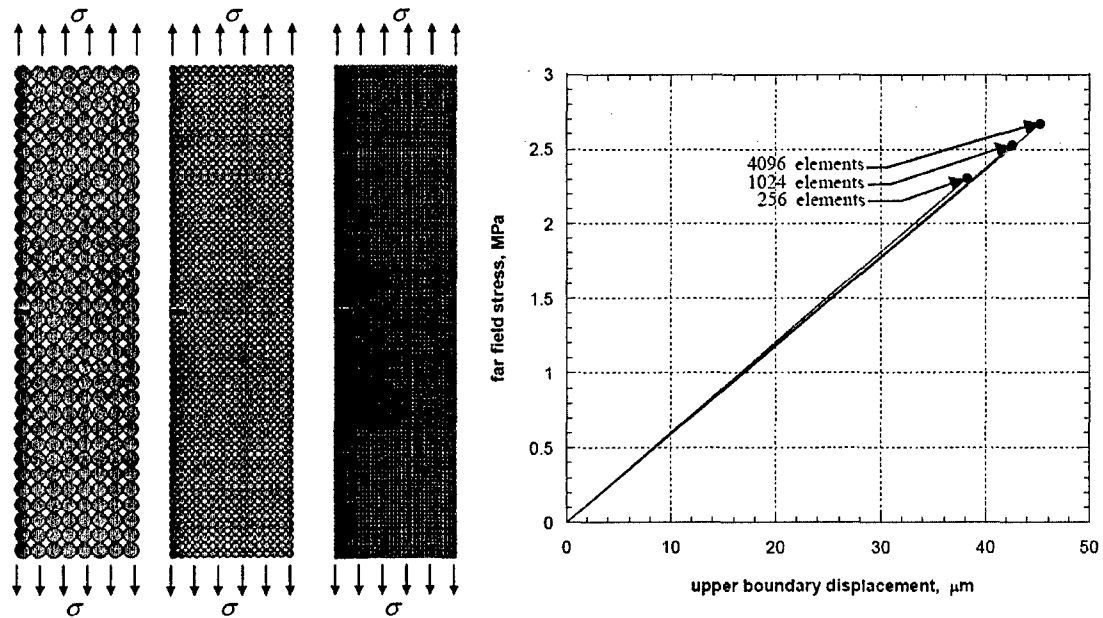


Figure 4.3 Convergence for crack growth in a DEM model of a cracked plate subjected to pure Mode I loading; solid circles in the plot represent the value of far field stress and displacement that cause unstable crack growth.

It is important to mention that an exact analytic solution for this problem (finite width plate with an edge crack) does not exist. This is due to the difficulty of finding a solution that satisfies the traction-free boundary conditions on the free edges. However, several numerical techniques have been developed in order to obtain very accurate approximate solutions to this type of problem. Such techniques include the Boundary Collocation Method, Green's Function Method, Asymptotic Approximation, and the Finite Element Method, among others. A commonly used solution to this problem, consisting of an finite width plate with an edge crack subjected to pure Mode I loading is given by (Gross and Strawley, 1964; Brown and Strawley, 1966)

$$\sigma_F = \frac{K_{Ic}}{\sqrt{\pi a}} \left[1.12 - 0.23(a/c) + 10.6(a/c)^2 - 21.7(a/c)^3 + 30.4(a/c)^4 \right]^{1/2} \quad (4.3)$$

where σ_F is the value of the far field stress that causes the crack to propagate unstably across the plate, a is the crack length ($= 0.03125$ m) and c is the width of the plate ($a/c = 1/8$ for all the models of Figure 4.3). Equation 4.3 was obtained by a least square fitting to data obtained by the Boundary Collocation Method, which is accurate to within 0.5 % for $a/c \leq 0.6$. Using the parameters cited earlier, Equation 4.3 provides $\sigma_F = 2.61$ MPa. The extrapolated DEM solution overpredicts the solution in Equation 4.3 by about 6.5 %. While part of this disagreement may be due to error in the Richardson extrapolation and the error in Equation 4.3 itself, it is nonetheless clear that the DEM results are converging to a value that is greater than the exact solution. As mentioned before, the value of the tangential spring stiffness influences the result, and it is likely that the use of Equation 4.2 for the tangential stiffness is inadequate. Another potential reason for this disagreement involves the incorrect fracture energy release rate obtained by using the present approach for contact stiffness and failure criterion. This will be explained in more detail in Section 5. While we view the agreement between DEM and the exact solution as good, additional work was needed in order to improve the accuracy of the DEM results. Nevertheless, the proposed failure criterion based on the fracture toughness of the material is superior and better suited for problems with existing cracks than a criterion based on the material's tensile strength, the results of which fail to converge.

5. General criterion for DEM interelement failures

In Section 3, a criterion for contact failure was developed as a function of element size and the material's fracture toughness, and convergence results presented in Section 4 revealed that for a model of a plate with an edge crack (using a simple cubic assembly), this criterion produced results which, while in very good agreement with the exact solution, they appeared to converge to a far field stress that was slightly higher. This section describes an enhanced failure criterion that appears to provide convergence, while allowing for failure according to the maximum principal stress failure criterion for uncracked media, and failure according to fracture mechanics for media with cracks.

Maximum Principal Stress Failure Criterion

In a DEM model with no initial flaws, where the fracture toughness is a constant material property, a failure criterion based on fracture mechanics and the material's fracture toughness will be inappropriate and will overpredict a structure's strength compared to the maximum principal stress criterion. Due to the similarity of the discrete element method with molecular dynamics, the fracture toughness will vary depending on the molecular (element) lattice. As such, since there are no guaranties that, in the limit of mesh refinement, that a DEM model will have flaws greater than the critical crack size for the material being modeled, hence we have developed an alternate criterion that automatically allows failure to be dictated by the ultimate tensile strength of the material, σ_{ult} , or the material's fracture toughness, K_{Ic} , as appropriate.

Fracture Energy Failure Criterion

Figure 5.1 shows a cracked specimen before and after an infinitesimal crack extension Δa . The energy release rate in a homogeneous, isotropic linear elastic material is determined by calculating the total work balance per unit thickness for extending a crack a distance Δa . Therefore,

$$G = \frac{1}{\Delta a} \int_0^{\Delta a} \int_0^{\delta^f} \sigma_{yy} d\delta dx \quad (5.1)$$

where δ^f is the crack opening displacement at position x behind the crack tip after crack extension Δa , and σ_{yy} is a function of both position x and the crack opening displacement δ behind the crack tip.

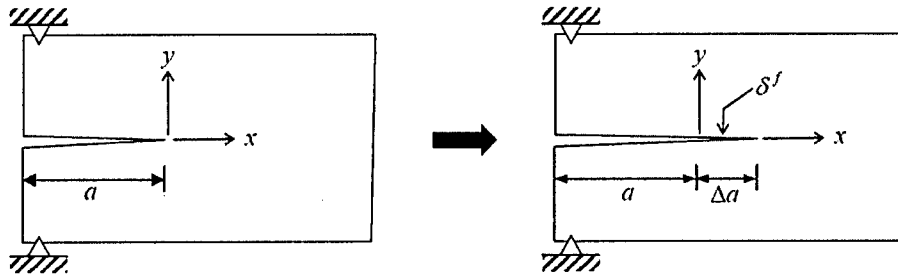


Figure 5.1 Specimen configurations before and after crack advance Δa .

Solving Equation 5.1 and taking the limit as $\Delta a \rightarrow 0$ yields the well known relationship between energy release rate and stress intensity factor K_I

$$G = \frac{K_I^2}{E^*} \quad (5.2)$$

In the present work, it will be assumed that the energy required to fracture an isotropic material is independent of the mode of fracture. Therefore, the fracture energy G_f or critical energy release rate is then given by Equation 5.2 when the value of K_I reaches the material's fracture toughness K_{Ic} . That is,

$$G_f = \frac{K_{Ic}^2}{E^*} \quad (5.3)$$

In DEM, Equation 5.1 simplifies since Δa is equal to the element diameter and therefore σ_{yy} is averaged by dividing the contact force by the diameter and thickness of the DEM element. Moreover, the crack opening displacement is also averaged over the diameter of the element and consists of the stretch of the normal direction spring in the crack tip contact. Therefore, in the present approach, the critical energy release rate is obtained by computing the area under the curve of σ_{yy} vs. δ at contact failure. For instance, Figure 5.2 shows the σ_{yy} vs. δ behavior when Equation 3.10 is used as a criterion for normal contact failure, and computes the fracture energy for this condition. As shown in the analysis in Figure 5.2, for a simple cubic assembly ($K_n = Et$), the obtained fracture energy will be

$$G_f = \frac{K_{Ic}^2}{\pi E} \quad (5.4)$$

which is different from the result in Equation 5.3. More importantly, this result shows that in order to have the correct critical energy release rate using Equation 3.10, the normal contact stiffness at the crack tip must be reduced by a factor of π .

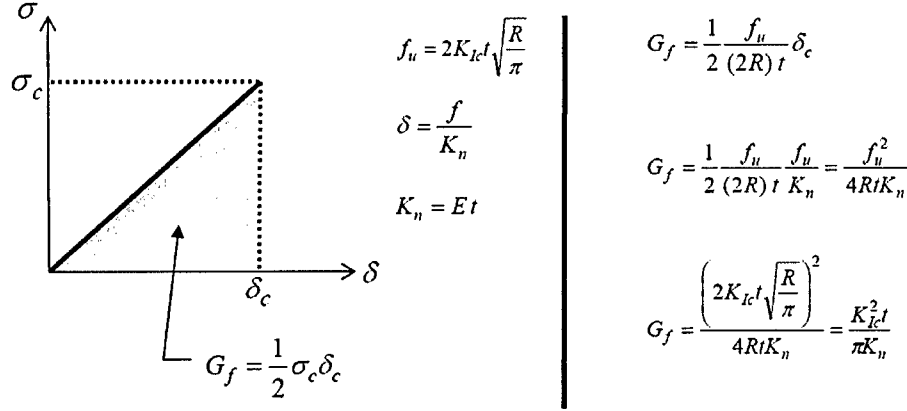


Figure 5.2 DEM Fracture energy computation using Equation 3.10 for contact failure.

Another important issue to consider is that the criterion in Equation 3.10 considers only Mode I cracking, where there is no force being carried by the tangential spring at the crack tip contact. Since in a two-dimensional simulation both Modes I and II can be present simultaneously in a contact, especially for close-packed and irregular discretizations, a fracture criterion should be developed to account for this type of loading where both the normal and tangential springs at the crack tip contact are being deformed.

In what follows, both a DEM flaw-free medium and a DEM cracked medium will be considered in order to develop a combined criterion for contact failure where the ultimate tensile strength of the material is used together with the material's fracture toughness to model crack tip contact failures.

DEM Flaw-Free Medium

Returning to the DEM unit cell, shown in Figure 5.3, we can obtain both the normal and tangential contact forces as a function of the applied uniaxial tensile stress in the unit cell. When the applied stress approaches the material's tensile strength σ_{ult} , using the unit cell results for normal and tangential contact stiffness, these forces are

$$f_n^{crit} = \frac{(Rt)\sigma_{ult}}{2(1-\nu^*)} \left(\sqrt{3} - \frac{\nu^*}{\sqrt{3}} \right) \quad (5.5)$$

$$f_t^{crit} = \frac{(Rt)\sigma_{ult}}{2(1-\nu^*)} (1 - 3\nu^*) \quad (5.6)$$

These critical forces for a close-packed assembly are analogous to the criterion leading to Equation 3.5, which is only based on the tensile strength of the material.

For a flaw-free medium, contact normal and tangential forces will reach the critical forces given by Equations 5.5 and 5.6 simultaneously and then the model will reach the ultimate tensile strength of the material. Regardless of the material's fracture toughness, the contact forces should not exceed those given by Equations 5.5 and 5.6.

Otherwise, the model's tensile strength will be greater than the material's tensile strength. However, a DEM cracked medium presents a different scenario for ultimate failure, as follows.

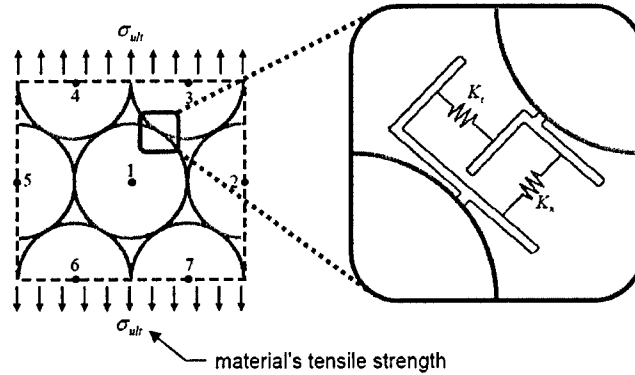


Figure 5.3 DEM unit cell used for determination of critical contact forces.

DEM Cracked Medium

When cracks are present, the contact forces at the crack tip reach the critical forces given by Equations 5.5 and 5.6 relatively quickly during loading since stresses at a DEM crack tip become infinite in the limit of mesh refinement. However, it is proposed that complete failure should not occur before the contact achieves the material's fracture energy G_f . In order to satisfy this condition, the stress-displacement curve shown in Figure 6.7 is adopted for both the normal and tangential contact at the crack tip.

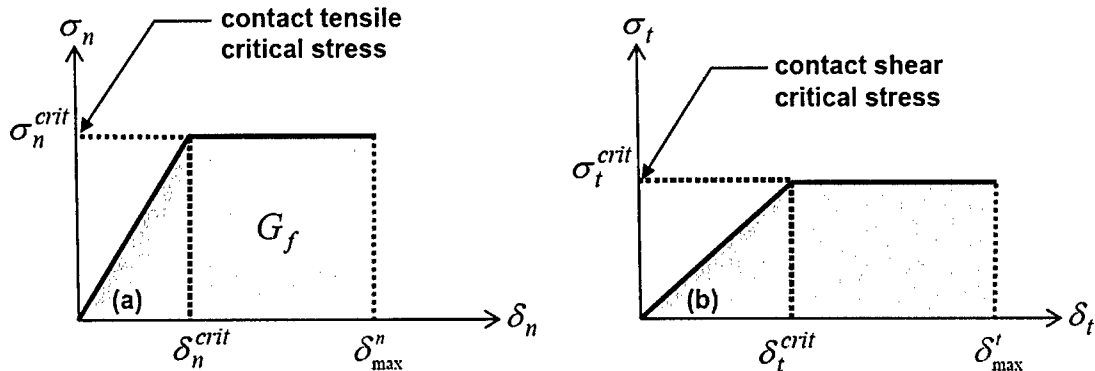


Figure 5.4 DEM contact stress-displacement behavior and fracture energy.

As shown in Figure 5.4, the contact springs (both normal and tangential) behave linearly up to the point where the forces satisfy Equation 5.5 or Equation 5.6 for the normal and tangential springs, respectively. Once these forces are reached, the behavior is proposed to be plastic until the area under the stress-displacement curve for the normal spring, shown in Figure 5.4(a), reaches the fracture energy of the material, given by Equation 5.3. It should be noted that the area under the curve in Figure 5.4(a) is the minimum energy lost, as energy may also be stored in the tangential direction of the contact.

The maximum normal displacement δ_{\max}^n is obtained by computing the area under the curve in Figure 5.4(a) and equating this to the material's fracture energy G_f . Therefore, the maximum normal displacement is given by

$$\delta_{\max}^n = \frac{K_{Ic}^2}{\sigma_n^{crit} E^*} + \frac{\delta_n^{crit}}{2} \quad (5.7)$$

where

$$\sigma_n^{crit} = \frac{f_n^{crit}}{2Rt} = \frac{\sigma_{ult}}{4(1-\nu^*)} \left(\sqrt{3} - \frac{\nu^*}{\sqrt{3}} \right) \quad (5.8)$$

$$\delta_n^{crit} = \frac{f_n^{crit}}{K_n} = \frac{R\sigma_{ult}}{2E^*} (3 - \nu^*) \quad (5.9)$$

Therefore, Equation 5.7 gives a displacement-based failure criterion, where the maximum displacement is a function of the material's tensile strength, elastic modulus, Poisson's ratio, and fracture toughness. Since contact stresses are computed using the radius of the elements in contact, the failure criterion is also element size dependent. It should be noted that if unloading occurs in the contact after it has reached the plastic range, the slope of the unloading force-displacement curve will be equal to the initial slope (K_n and K_t for the normal and tangential stiffnesses, respectively).

Convergence

To test the failure criterion given in Equation 5.7, three DEM models representing a plate with a crack subjected to pure Mode I loading were developed. The models, shown in Figure 5.5, consist of 1172, 4713, and 18899 elements, respectively, arranged in a close-packed assembly. The material modeled by these DEM meshes has elastic modulus $E = 29.7$ GPa, Poisson's ratio $\nu = 0.3$, ultimate tensile strength $\sigma_{ult} = 3.44$ MPa, and fracture toughness $K_{Ic} = 1.0$ MPa \sqrt{m} (i.e., concrete).

The results of the DEM simulations are also shown in Figure 5.5, where the hollow data points represent values of the far field stress that cause the crack to propagate unstably across the model. As mentioned before, using Equation 4.3 for this problem gives $\sigma_F = 2.61$ MPa. Applying Richardson extrapolation to the results of these three models provides an estimate of $\sigma_{ult} = 2.595$ MPa as the value of the far field stress that the DEM models will converge to, which is within 0.5% of the solution in Equation 4.3, which could be in error by as much as 0.5%. Therefore, the proposed criterion for contact failure appears very promising.

Applying Equation 4.1 to the results of the three models, a convergence rate $p = 1.8$ (almost quadratic) was obtained, which is a reasonable value and is encouraging. The models shown in Figure 5.5 were also developed with no initial crack, and all three models essentially carried a maximum stress of $\sigma = 3.44$ MPa (independent of model discretization), which agrees with the value of the ultimate tensile strength of the material σ_{ult} . Therefore, the proposed method provides excellent results regardless of the type of failure (fracture toughness or ultimate tensile strength).

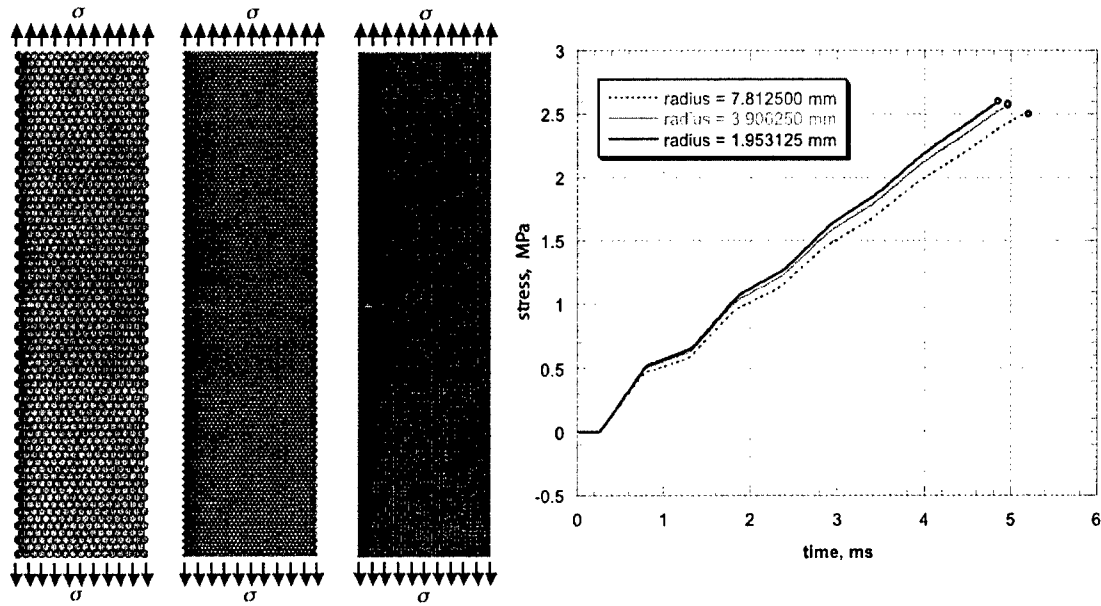


Figure 5.5 Convergence for crack growth in a DEM model of a cracked plate subjected to pure Mode I loading; hollow data points in the plot represent the value of far field stress and displacement that cause unstable crack growth.

6. DEM for modeling concrete penetration

One of the objectives of our study was to use DEM for modeling impact and penetration events, with special interest on concrete members. An important issue is the influence of strain rate effects on material properties such as the tensile strength and elastic modulus, among others. Thus, material properties determined from static tests may not be applicable to impact situations without adjustments to account for the rate of loading. In a study of fracture of concrete under uniaxial impact tensile loading, Zielinski (1982) observed that the elastic stiffness, stress levels at failure, and deformation capacity were all higher when compared to static uniaxial tensile tests. In fact, for dynamic loading, the ultimate compressive strength can be more than doubled (Bischoff and Perry 1991), whereas the ultimate uniaxial tensile strength increases by multiples of 5 to 7 at very high strain rates (Ross et al. 1996). In Tavarez (2005), we review some of the literature on strain rate effects with special interest in concrete. We also review models that have been proposed by Tang, Malvern, and Jenkins (1992), Dilger, Koch, and Kowalczyk (1984), Mikkola and Sinisalo (1982), and Soroushian, Choi, and Alhamad (1986), among others.

Tensile Strength

Far less dynamic testing has been carried out on concrete in tension than in compression (Fu et al. 1991), and therefore there is insufficient data available to allow the derivation of reliable empirical expressions. Suaris and Shah (1983) suggested that rate sensitivity is considerably more pronounced in tension and flexure than in compression. Tedesco et al. (1989) carried out split Hopkinson bar tests on direct tensile specimens and

observed ratios of dynamic to static strengths of up to 3.6 at strain rates of approximately 8 s^{-1} . Weerheim and Reinhardt (1989) carried out tensile loading of notched specimens using a split Hopkinson bar and found a ratio of dynamic to static tensile strength of approximately 2 at a stress rate of 10^4 MPa/s , rising sharply to 4.5 at $2 \times 10^5 \text{ MPa/s}$. Brara et al. (2001) conducted experiments on concrete specimens in tension using a new experimental technique base on the Hopkinson bar principle and the spalling phenomenon, and concluded that for strain rates of approximately 120 s^{-1} , the dynamic tensile strength exceeds the quasi-static value by approximately an order of magnitude. John et al. (1987) proposed a model to predict the dynamic tensile strength for concrete using three material parameters: fracture toughness K_{Ic} , critical crack tip opening displacement $CTOD_c$, and Young's Modulus E . In their approach, K_{Ic} and E are assumed to be rate independent while $CTOD_c$ is assumed to decrease exponentially with the logarithm of the relative strain rate. The dynamic tensile strength is then computed using the following formula

$$(\sigma_{ult})_d = 1.4705 \cdot \frac{K_{Ic}^2}{E \cdot (CTOD_c)_d} \quad (6.1)$$

where the dynamic critical crack tip opening displacement is calculated as

$$(CTOD_c)_d = CTOD_c \cdot e^{-0.00075(\bar{\epsilon})^{0.65}} \quad (6.2)$$

$$\bar{\epsilon} = \log\left(\frac{\dot{\epsilon}}{\dot{\epsilon}_0}\right) \quad (6.3)$$

where the static critical crack tip opening displacement $CTOD_c = 0.0005 \text{ in.}$ and the quasi-static strain rate $\dot{\epsilon}_0 = 30 \times 10^{-6} \text{ s}^{-1}$.

Elastic Modulus

The limited data available suggest that increases in Young's modulus with strain rate are far less pronounced than increases in compressive strength. Using the data available from the literature, Williams (1994) proposed the following formula for the ratio of dynamic to static Young's modulus (E_{cd}/E_{cs})

$$\frac{E_{cd}}{E_{cs}} = 1.325\dot{\epsilon}^{0.0234} \quad \dot{\epsilon} \geq 6 \times 10^{-6} \quad (6.4)$$

However, due to the very wide scatter of the data, Williams stated that this relationship should be treated with caution. The following section will discuss the actual equations that were incorporated into our DEM method to treat strain rate effects.

Strain Rate Effects Formulae used in the DEM Method

Although more work needs to be done in developing models for rate of loading effects for concrete, and in testing applications of these to DEM models, we have employed the following. Klepaczco (1990) proposed a criterion to determine the dynamic tensile strength of concrete based on experimental results relating fracture stress σ_F and critical loading time t_{c0} . This criterion was proposed for high strain rates (higher than 20

s⁻¹) and has the advantage of being based on some physical notion taking into account the thermally activated rate process. The criterion in the integral form is expressed as

$$t_{c0} = \int \left(\frac{\sigma_F(t)}{\sigma_{ult}} \right)^{\alpha(T)} dt \quad (6.5)$$

where σ_{ult} , t_{c0} , and $\alpha(T)$ are three material constants at a given temperature T . The parameter α is temperature dependent and is related to the activation energy of material separation. The parameter t_{c0} is the longest critical time at which $\sigma_F(t_{c0}) = \sigma_{ult}$, where σ_{ult} is the quasi-static tensile strength. For a linearly proportional loading, the integral form of the criterion in Equation 6.5 takes the following form

$$\sigma_F = \left[(\alpha + 1) t_{c0} E \sigma_{ult} \right]^{\frac{1}{\alpha+1}} \dot{\epsilon}^{\frac{1}{\alpha+1}} \quad (6.6)$$

where E is the Young's modulus (under static conditions) and $\dot{\epsilon}$ is the strain rate. According to experimental results on wet concrete, Brara et. al (2001) found these parameters to be: $\alpha = 0.95$ and $t_{c0} = 50 \mu\text{s}$. Comparing the results of Equation 6.6 with data obtained from the literature, it was found that the formula fits very well to the majority of experimental data and can also be used for smaller strain rate values (but greater than 0.75 s^{-1}) and still obtain reasonable results. As such, the expression in Equation 6.6 was adopted in our work to obtain the dynamic tensile strength as a function of strain rate for strain rates greater than 0.75 s^{-1} . For smaller strain rates, the static value of tensile strength was used. In our DEM code, the normal strain rate is computed at each time step using

$$\dot{\epsilon} = \frac{|\mathbf{v} \cdot \mathbf{n}|}{L_0} \quad (6.7)$$

where \mathbf{v} is the relative velocity vector between two DEM particles, \mathbf{n} is the normal unit vector, and L_0 is the initial center-to-center distance between bonded DEM elements.

It is well known that enhancement of elastic modulus due to strain rate effects is less significant than that of tensile strength and compressive strength (Williams, 1994; Koh et al. 2001). We use the following expressions to determine the dynamic elastic modulus as a function of strain rate in compression and tension, respectively (CEB, 1988):

$$\frac{E_{cd}}{E_{cs}} = \left(\frac{\dot{\epsilon}}{\dot{\epsilon}_0} \right)^{0.026} \quad (6.8)$$

$$\frac{E_{td}}{E_{ts}} = \left(\frac{\dot{\epsilon}}{\dot{\epsilon}_0} \right)^{0.016} \quad (6.9)$$

where the subscripts c , t , d , and s denote compressive, tensile, dynamic, and (quasi-) static states, respectively. The quasi-static strain rate is taken as $\dot{\epsilon}_0 = 30 \times 10^{-6} \text{ s}^{-1}$.

It has also been observed that the fracture toughness K_{Ic} increases as the rate of applied load is increased. Mindess et al. (1987) conducted experiments on single-edge

notched concrete beams loaded dynamically in 3-point bending, using an instrumented drop weight impact machine in order to study the effect of the load rate on the fracture energy and fracture toughness of the material. It was found that fracture toughness values and fracture energies under impact loading were much higher (approximately an order of magnitude) than those obtained in static tests.

An experimental investigation of mode I fracture of concrete was conducted by Lambert and Ross (2000) under the dynamic loading of a split Hopkinson pressure bar. Fracture specimens in the form of notched-cavity splitting tension cylinders were subjected to stress wave loading that produced strain rates up to 10 s^{-1} . A very good linear relationship between fracture toughness and strain rate was found over a strain rate range of 1 s^{-1} to 8 s^{-1} . The fracture toughness increased by a factor of approximately 3 when the strain rate increased from 1 s^{-1} to 8 s^{-1} . However, this linear trend was not suggested as a global trend for the entire strain rate spectrum. It is important to mention that the analysis of fracture toughness data under high rates of loading, or under impact loading is complex. For instance, the dynamic fracture toughness is dependent on the crack velocity, which may vary considerably as the crack propagates. Therefore, due to the lack of available data for K_{Ic} at higher strain rates, it was decided instead to apply strain rate effects to the material's fracture energy G_f , since the failure criterion is primarily based on this quantity. As such, it was also assumed that the material's dynamic fracture energy changes in the same fashion as the dynamic ultimate tensile strength as a function of strain rate. That is, we used the following expression to determine the dynamic fracture energy as a function of strain rate

$$(G_f)_d = \xi (G_f)_s \quad (6.10)$$

where the factor ξ is the ratio of dynamic to static tensile strength for the given strain rate. This factor is directly applied to the computed static fracture energy (Equation 5.3) rather than to K_{Ic} so that strain rate effects do not become excessive from computing the square of the dynamic fracture toughness in order to determine the dynamic fracture energy using the relationship in Equation 5.3.

DEM Compression Behavior – Material Densification

One aspect of our DEM method that has not yet been described is the compression behavior of the medium. Often, the possibility of compression failures in DEM models is neglected, with the main emphasis being on tensile failures. However, in problems involving penetration, extremely high compressive stresses are produced, and the possibility of compressive failure should be included. Experimental results have shown that concrete targets exhibit what is referred to as “medium densification” for the material ahead of the projectile, which is another local source of energy absorption. There is likely a considerable amount of energy that is absorbed due to this phenomenon and this is incorporated to some extent into the method we have developed.

To illustrate our DEM approach, consider the bonded elements shown in Figure 6.1(a). The cluster, which is attached to a boundary that could be a fixed support or another DEM element, consists of elements of initial radius r_0 . As shown in Figure 6.1, the initial (equilibrium) distance between the elements is given by d_0 . Therefore, contact

or separation is determined by comparing the sum of the radii of the elements with the initial distance d_0 (for bonded contacts).

When the contact is in compression, the normal-direction spring behaves in a linear fashion using the normal spring stiffness given in Equation 3.1 for plane stress and plane strain. However, we propose that when the contact achieves a critical compressive stress, the equilibrium distance d_0 will then be changed to d_0^* , as shown in Figure 6.1(b), and the contact normal force will behave in a plastic manner in order to account for non-recoverable material densification. Therefore, further compression (or separation) of the contact will be measured relative to this new equilibrium configuration given by d_0^* . In essence, the DEM elements are allowed to overlap. Once the medium has reached total compaction, the contact will behave again in a linear fashion, with a normal contact stiffness equal to its initial stiffness.

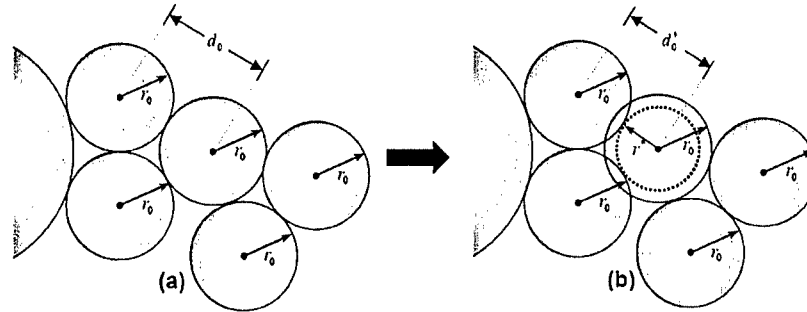


Figure 6.1 DEM treatment of compressive behavior and material densification.

Rather than allowing DEM elements to overlap, the densification process described here could also be implemented by allowing the element radius to reduce from r_0 to r^* , as suggested in Figure 6.1(b), and increasing the element density in order to conserve the element's mass. However, this latter approach was not used in our study because reduction of the element radius will most likely affect other contacts associated with this element (i.e., contact separation will occur, as shown in the figure). In the approach we use wherein some DEM elements are allowed to overlap, other contacts associated with the element (which may not be at a critical compressive stage) will be unchanged, and material densification will automatically be obtained because of the overlap between appropriate DEM elements. This technique is also, in some aspects, analogous to establishing a nonlinear equation of state (EOS) for the medium.

In order to determine the compressive critical contact stress, the results obtained from the DEM unit cell shown in Figure 5.3 were used. The critical normal force given in Equation 5.5 is then applied, using the value of maximum compressive strength f'_c instead of the maximum tensile strength σ_{ult} . The critical compressive contact force $(f_n^{crit})_c$ is then given by

$$(f_n^{crit})_c = \frac{(Rt)f'_c}{2(1-\nu^*)} \left(\sqrt{3} - \frac{\nu^*}{\sqrt{3}} \right) \quad (6.11)$$

Since the material's compressive strength is now included, this parameter will also be dependent on the strain rate $\dot{\epsilon}$. The dynamic compressive strength will be determined using (CEM, 1988)

$$\frac{f'_{cd}}{f'_{cs}} = \left(\frac{\dot{\epsilon}}{\dot{\epsilon}_0} \right)^{1.026\alpha} \quad \text{for} \quad \dot{\epsilon} \leq 10 \text{ s}^{-1} \quad (6.12)$$

$$\frac{f'_{cd}}{f'_{cs}} = \gamma (\dot{\epsilon})^{1/3} \quad \text{for} \quad \dot{\epsilon} > 10 \text{ s}^{-1} \quad (6.13)$$

where

$$\log \gamma = 6.15\alpha - 0.492 \quad (6.14)$$

$$\alpha = 1 / \left(5 + 3f'_c / 4 \right) \quad (6.15)$$

and f'_c is the static compressive strength in MPa at a quasi-static strain rate $\dot{\epsilon}_0 = 30 \times 10^{-6} \text{ s}^{-1}$. Figure 6.2 shows the ratio of dynamic to static compressive strength of concrete as a function of strain rate. The strain rate has a smaller effect on compressive strength than on the tensile strength of the material.

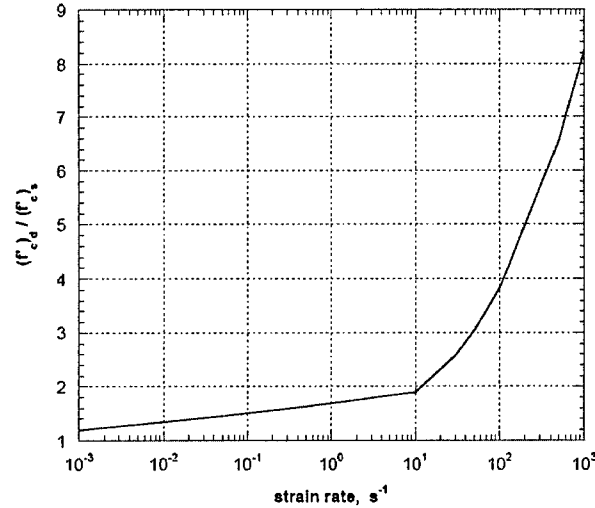


Figure 6.2 Strain rate effect on ultimate compressive strength.

It is important to mention that due to the lack of available data for validation, it was not clear how to choose or determine the parameters that govern the compaction phase. These parameters are the compaction stiffness and the strain at full compaction and they were chosen somewhat arbitrarily. As mentioned before, it was assumed that in the compaction phase the contact behaves plastically and it will continue to do so until the distance between the element centers (given by d_0^*) reaches the DEM element radius R . When this happens, it is assumed that the material has reached full compaction and therefore, it will continue to have a normal stiffness equal to the initial stiffness K_n .

Additional work is required to validate the parameters chosen for this compaction phase and to gain more confidence in their use. Nevertheless, as will be shown later, it is an essential phenomenon to incorporate in a high speed penetration event, especially for concrete members.

7. DEM simulation of concrete penetration

This work developed a new approach for using the DEM method to assess local damage to concrete structures subjected to extreme loading. Currently, damage to reinforced concrete structures is evaluated mainly with empirical formulas derived from various types of impact tests. DEM simulation results are presented here with a comparison with available formulas for predicting penetration, scabbing thickness, and perforation thickness in plain concrete targets. A limitation to our numerical DEM implementation is that real life penetration events are three dimensional, whereas our DEM model is presently two dimensional. Tavares (2005) describes a calibration process so that qualitative comparisons can be made between our two dimensional simulations and the available empirical formulas. We note that for two dimensional simulations, no calibration process is needed, but unfortunately, data for structure behavior under extreme loading conditions is not as well developed. For more accurate applications to projectile penetration, a three dimensional implementation of our results is needed, and this may be considered in future work.

Figure 7.1 shows the DEM model used for simulating penetration events. The concrete member consists of 12000 DEM elements and is cantilever-supported at both ends. The model has a length of 96 in. with a depth of 30 in., and is assumed to be in plane strain conditions. Therefore, all quantities (density, contact stiffness, stresses, etc.) are computed per unit thickness. The projectile is steel and consists of 351 DEM elements and was constructed using a close-packed assembly. The projectile has a width (diameter) of 3.5 in. and its density was determined so that its total weight is 15 lbs. The following subsections provide more details about the properties used for both materials.

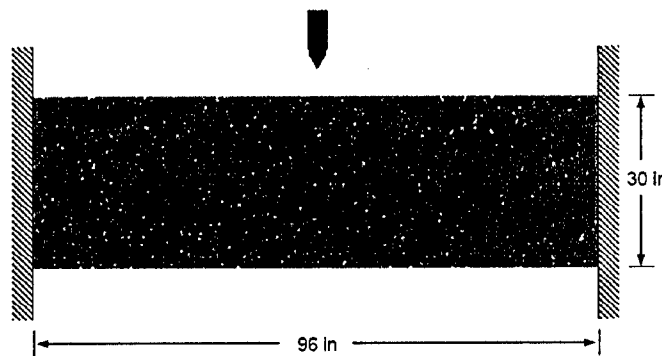


Figure 7.1 DEM discretization for modeling penetration in a concrete member.

Concrete Target

Table 7.1 shows the DEM model details and material properties for the concrete target used in all simulations. All material properties reported in this table are quasi-static

values. Such values are then used in the code to compute the respective dynamic properties as a function of strain rate.

Table 7.1 Concrete properties used in DEM model.

Density (ρ)	DEM element radius (R)	Elastic modulus (E)	Poisson's ratio (ν)	Tensile strength (σ_{ult})	Compressive strength (f'_c)	Fracture toughness (K_{Ic})
2.17×10^{-4} lb-s ² /in	0.25 in.	3,122 ksi	0.2	300 psi	3000 psi	910 psi-s ^{1/2}

Steel Projectile

Table 7.2 shows the DEM model details and material properties used for the steel projectile used in the analysis. It is important to mention that even though the projectile is deformable, it does not have failure capabilities incorporated for it. This was decided due to the relative coarse mesh (resulting in a somewhat rough surface) and assembly used for the projectile model. Moreover, experimental data show that most projectile damage phenomena is due to thermodynamic issues and therefore, since this aspect of deformation was not incorporated into the model, it was decided not to include erosion or failure of the projectile.

Table 7.2 Projectile properties used in DEM model.

Effective Density (ρ)	DEM element radius (R)	Elastic modulus (E)	Poisson's ratio (ν)	Projectile diameter (D)	Projectile weight (W)
2.43×10^{-3} lb-s ² /in	0.15544 in	29,000 ksi	0.3	3.5 in	15 lb

DEM Analysis Procedure

The velocity of the projectile was varied in the numerical simulations, and depending on the impact velocity, different behaviors were observed. However, in order to compare the numerical results produced by the 2-D DEM code used in this work with available empirical formulas for penetration, scabbing, and perforation of concrete targets, which are based on 3-D experimental results, the following approach was taken. After creating the DEM model shown in Figure 7.1, it was necessary to calibrate the model to determine the effective tensile strength and fracture toughness of the medium. According to the available empirical formulas and the given material properties, for the model considered here, the penetration depth should be approximately 5 inches for a projectile velocity of 500 ft/s, without producing scabbing in the back face of the target. As such, the initial velocity of the projectile in the DEM model was set to $V_0 = 500$ ft/s, and the calibration parameter was varied until a penetration depth of approximately 5 inches was obtained. Once this calibration was completed, subsequent simulations were carried out with no recalibrations. In the subsequent simulations:

- The velocity of the projectile was gradually increased in order to produce scabbing, and then penetration in the concrete target.
- The scabbing and penetration velocities obtained from the numerical simulations were then compared to the results obtained using the available empirical formulae.

According to the DEM model parameters, the required time step for the simulations was approximately $\Delta t = 8.9 \times 10^{-8}$ seconds. Due to the number of elements in the model, an average running time of approximately 15 hours on a Unix workstation was needed for a simulation time of approximately 10 ms, which was the simulation time required for a complete penetration event.

DEM Simulation Results

Figure 7.2(a) shows the projectile at its maximum depth of penetration, which is approximately 5.05 in., and Figure 7.2(b) shows the vertical position of the projectile tip as a function of time. The hollow data point indicates when the projectile impacts the top of the beam.

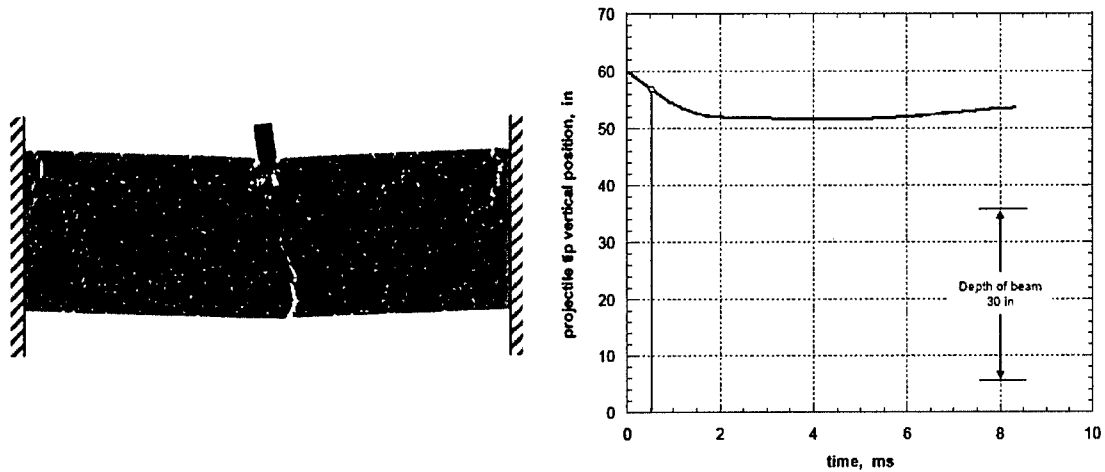


Figure 7.2 Projectile maximum penetration and tip vertical position as a function of time.

The figure also shows the depth of the beam, which is shown in the scale of the figure (i.e., 30 in.). As seen in Figure 7.2(a), there were flexural cracks resulting in global deformation in the target, which makes it difficult to determine the actual penetration depth relative to the target. Nevertheless, the results obtained in this simulation agree very well with the NDRC prediction.

Figure 7.3 shows the results of the different available empirical formulae to determine the scabbing thickness h_s of a concrete target subjected to projectile penetration. As defined earlier, the scabbing thickness is the minimum thickness required to prevent scabbing in a concrete target.

Since it is a lengthy process to construct DEM models of different thickness, it was instead decided to determine the minimum projectile velocity required to induce scabbing in the model. In Figure 7.3, we see that for the 30 in. target thickness of our DEM model, the predicted values for scabbing thickness vary from 750 ft/s to 1250 ft/s. In order to determine the “scabbing velocity” in our DEM model, the projectile velocity was increased in intervals of 50 ft/s until scabbing was produced in the model.

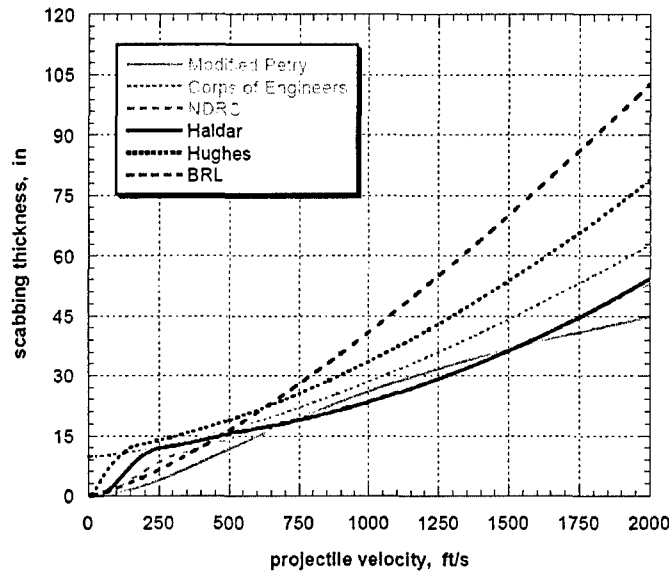


Figure 7.3 Calculated scabbing thickness (using data listed in Tables 7.1 and 7.2).

Figure 7.4 shows scabbing in the DEM model for a projectile impact velocity of $V_0 = 850$ ft/s. There was no scabbing at a velocity of 800 ft/s (only a large flexural crack that led to ultimate fracture of the beam), and therefore it was determined that the “scabbing velocity” for the model is 850 ft/s which falls within the predicted values of the available empirical formulas. The snapshot at Stage 4 in Figure 8.8 shows the maximum penetration in the model.

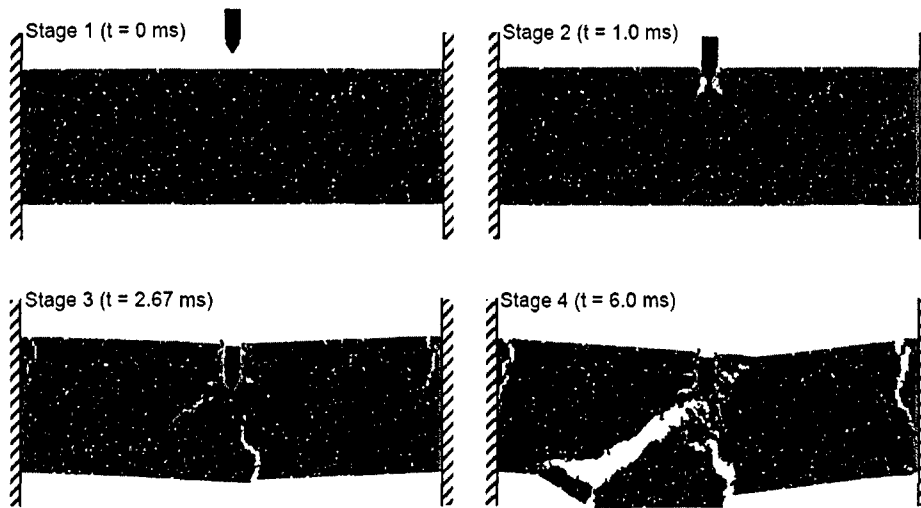


Figure 7.4 Scabbing in concrete target.

The scabbing velocity for the model agrees very well with the prediction of the BRL formula, which predicts a scabbing velocity of $V_0 = 760$ ft/s. We note that this equation is the only one among the many empirical formulas that does not rely on the penetration depth x_f to determine the scabbing thickness. According to the BRL equations, the scabbing thickness is determined from the perforation thickness. It is important to

mention that the addition of the nonlinear compression behavior decreases the degree of brittleness in the model and therefore scabbing is produced at a higher velocity than might actually occur. As seen in Figure 7.4 (stage 4), considerable penetration occurred in the model before any scabbing was present, suggesting that when it did occur, there were other factors that contributed to it such as overall deformation and the development of flexural and shear cracks.

Figure 7.5 shows the results of the different available empirical formulae to determine the perforation thickness h_p of a concrete target, where the perforation thickness is the minimum thickness required to prevent perforation in a concrete target. Analogous to the procedure done for scabbing, it was decided to determine the minimum velocity required to completely perforate the target. This velocity is also known as the *ballistic limit*. In Figure 7.5, we can see that for a target thickness of 30 in., the predicted values for perforation thickness vary from approximately 1000 ft/s to 1500 ft/s. Figure 7.6 shows a DEM model where full perforation was obtained. As in the procedure done to determine the scabbing velocity, the projectile velocity was increased in intervals of 50 ft/s until full perforation was achieved in the model. This was obtained for an impact velocity of 1150 ft/s, which again falls within the range of predictions from the available empirical formulas.

The perforation velocity obtained from the DEM simulations agrees particularly well with the prediction from the BRL equation (shown in Figure 7.5), which directly predicts the perforation thickness without using the penetration depth x_f or the scabbing thickness h_p . Although the results obtained from the simulations presented in this chapter are very encouraging, additional work is required so that more confidence is gained in the use of the proposed approach to predict local damage in concrete targets due to projectile impact.

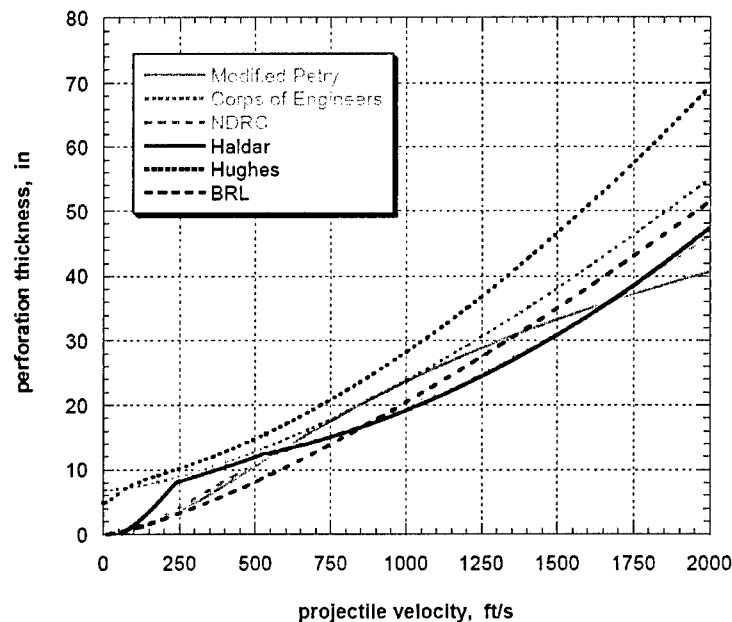


Figure 7.5 Calculated perforation thickness (using data listed in Tables 7.1 and 7.2).

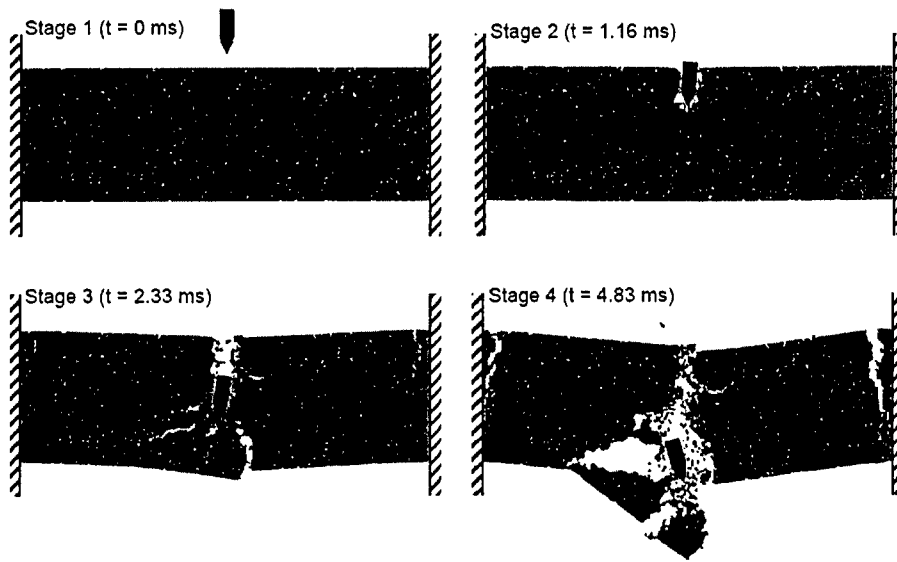


Figure 7.6 Perforation in concrete target.

Bibliography

- Anderson, T.L., *Fracture Mechanics – Fundamentals and Applications*, 2nd Ed., CRC Press, 1994.
- Bishoff, P.H. and Perry, S.H., "Compressive Behavior of Concrete at High Strain Rates," *Materials and Structures*, Vol. 24, 1991, pp. 425-450.
- Bolander, J.E. and Saito, S., "Discrete Modeling of Short-Fiber Reinforcement in Cementitious Composites," *Advanced Cement Based Materials*, Vol. 6, 1997, pp. 76-86.
- Brara, A., Camborde, F., Klepaczko, J.R. and Mariotti, C., "Experimental and Numerical Study of Concrete at High Strain Rates in Tension," *Mechanics of Materials*, Vol. 33, 2001, pp. 33-45.
- Brown, W.F., Jr., and Strawley, J.E., "Plane Strain Crack Toughness Testing of High Strength Metallic Materials," *ASTM Special Technical Publication*, No. 410, 1966.
- Camborde, F., Mariotti, C., and Donze, F.V., "Numerical Study of Rock and Concrete Behavior by Discrete Element Modeling," *Computers and Geotechnics*, Vol. 27, 2000, pp. 225-247.
- Cook, R.D., Malkus, D.S., and Plesha, M.E., *Concepts and Applications of Finite Element Analysis*, 3rd Edition, John Wiley & Sons, 1989.
- Dilger, W.H., Koch, R., and Kowalczyk, R., "Ductility of Plain and Confined Concrete under Different Strain Rates," *ACI Structural Journal, Proceedings*, Vol. 81, No. 1, Jan.-Feb 1984, pp. 73-81.
- Donze, F.V., Bouchez, J., and Magnier, S.A., "Modeling Fractures in Rock Blasting," *Int. J. Rock Mech. Min. Sci.*, Vol. 34, No. 8, 1997, pp. 1153-1163.
- Fu, H.C., Erki, M.A., and Seekin, M., "Review of Effects of Loading Rate on Reinforced Concrete," *ASCE Journal of Structural Engineering*, Vol. 117, No. 12, Dec. 1991, pp. 3660-3679.
- Gross, B. and Strawley, J.E., "Stress-Intensity Factors for a Single-Edge-Notch Tension Specimen by Boundary Collocation of a Stress Function," *NASA TN D-2395*, 1964.
- Heuze, F.E., Walton, O.R., Maddix, D.M., Shaffer, R.J., and Butkovich, T.R., "Analysis of Explosions in Hard Rocks: The Power of Discrete Element Modeling," *Comprehensive Rock Engineering - Analysis and Design Methods*, Vol. 2, 1993, pp. 387-413.
- John, R., Shah, S.P., and Jenq, Y.S., "A Fracture Mechanics Model to Predict the Rate Sensitivity of Model I Fracture of Concrete," *Cement and Concrete Research*, Vol. 17, 1987, pp. 249-262.
- Koh, C.G., Liu, Z.J., and Quek, S.T., "Numerical and Experimental Studies of Damage under Impact," *Magazine of Concrete Research*, No. 53, No. 6, 2001, pp. 417-427.
- Kun, F. and Herrmann, H.J., "A Study of Fragmentation processes using a Discrete Element Method," *Computer Methods in Appl. Mech. and Engr.*, Vol. 138, 1996, pp. 3-18.
- Lambert, D.E. and Ross, C.A., "Strain Rate Effects on Dynamic Fracture and Strength," *International Journal of Impact Engineering*, Vol. 24, 2000, pp. 985-998.
- Magnier, S.A. and Donze, F.V., "Numerical Simulations of Impacts using a Discrete Element Method," *Mechanics of Cohesive-Frictional Materials*, Vol. 3, 1998, pp. 257-276.
- Masuya, H., Kajukawa, Y., Nakata, Y., "Application of the Distinct Element Method to the Analysis of Concrete Members under Impact," *Nuclear Engineering and Design*, Vol. 150, 1994, pp. 367-377.
- Mikkola, M.J. and Sinisalo, H.S., "Nonlinear Dynamic Analysis of Reinforced Concrete Structures," *Proceedings, Interassociation Symposium on concrete under Impact and Impulsive Loading*, Berlin, 1982, pp. 534, 547.
- Mindess, S., Banthia, N., and Yan, C., "The Fracture Toughness of Concrete under Impact Loading," *Cement and Concrete Research*, Vol. 17, 1987, pp. 231-241.
- Mishra, B.K. and Thornton, C., "Impact Breakage of Particle Agglomerates," *International Journal of Minerals Processing*, Vol. 61, 2001, pp. 225-239.
- Potyondy, D.O., Cundall, P.A., and Lee, C.A., "Modeling Rock using Bonded Assemblies of Circular Particles," *Proceedings of the 2nd N. American Rock Mechanics Symposium, Montreal*, 1996, pp.1937-1944.
- Potyondy, P. and Cundall, P., "A Bonded-Particle Model for Rock," *International Journal of Rock Mechanics & Mining Sciences*, Vol. 41, 2004, pp. 1329-1364.
- Prochazka, P.P., "Application of Discrete Element Methods to Fracture Mechanics of Rock Bursts," *Engineering Fracture Mechanics*, Vol. 71, 2004, pp. 601-618.
- Ross, C.A., Jerome, D.M., Tedesco, J.W., and Hughes, M.L., "Moisture and Strain Rate Effects on Concrete Strength," *ACI Materials Journal*, Vol. 93, No. 3, May-June, 1996, pp. 293-300.

- Sawamoto, Y., Tsubota, H., Kasai, Y., Koshika, H., and Morokawa, H., "Analytical Studies on Local Damage to Reinforced Concrete Structures under Impact Loading by Discrete Element Method," *Nuclear Engineering and Design*, Vol. 179, 1998, pp. 157-177.
- Soroushian, P., Choi, K., and Alhamad, A., "Dynamic Constitutive Behavior of Concrete," *ACI Journal, Proceedings*, Vol. 83, No. 2, March-April, 1986, pp. 251-258.
- Suaris, W., and Shah, S.P., "Properties of Concrete Subjected to Impact," *ASCE Journal of Structural Engineering*, Vol. 9, No. 7, July, 1983, pp. 1727-1741.
- Tang, T., Malvern, L.E., and Jenkins, D.A., "Rate Effects in Uniaxial Dynamic Compression of Concrete," *ASCE Journal of Engineering Mechanics*, Vol. 118, No. 1, January, 1992, pp. 108-124.
- Tavarez, F.A., Discrete Element Method for Modeling Solid and Particulate Materials, Ph.D. Thesis, Department of Engineering Physics, University of Wisconsin - Madison, 2005.
- Tavarez, F.A., and Plesha, M.E., Discrete Element Method for Modeling Penetration, Structures Under Extreme Loading Symposium, 2004 ASME Pressure Vessels and Piping Conf., San Diego, CA, pp. 165-171, 2004.
- Tavarez, F.A., and Plesha, M.E., Discrete Element Method for Modeling Solid and Particulate Materials, *Int'l. Journal for Numerical Methods in Engineering*, submitted for publication, 2006.
- Tedesko, J.W., Ross, C.A., and Brunair, R.M., "Inelastic Analysis of the Dynamic Split Cylinder Test," *Proceedings, 4th International Symposium on the Interaction of Non-Nuclear Munitions with Structures*, Panama City Beach, FL, April, 1989, pp. 302-308.
- Weerheijm, J. and Reinhardt, H.W., "Modeling of Concrete Fracture under Dynamic Tensile Loading," *Proceedings, Symposium on Recent Developments in Fracture of Concrete and Rock*, Cardiff, 1989, pp. 721-729.
- Williams, M.S., "Modeling of Local Impact Effects on Plain and Reinforced Concrete," *ACI Structural Journal*, Vol. 91, No. 2, March-April 1994, pp. 178-187.
- Zielinski, A.J., "Fracture of Concrete and Mortar under Uniaxial Impact Tensile Loading," Doctoral Thesis, Delft University of Technology, 1982.
- Zubelewicz, A. and Bazant, Z.P., "Interface Element Modeling of Fracture in Aggregate Composites," *Journal of Engineering Mechanics*, Vol. 113, No. 11, 1987, pp. 1619-1630.
- CEB, Concrete Structures under Impact and Impulsive Loading, *Synthesis Report, Bulletin d'Information No. 187*. Comité Euro-International du Béton (CEB), Lausanne, 1988.

Publications resulting from this work:

- Tavarez, F.A., and Plesha, M.E., Discrete Element Method for Modeling Penetration, Structures Under Extreme Loading Symposium, 2004 ASME Pressure Vessels and Piping Conf., San Diego, CA, pp. 165-171, 2004.
- Tavarez, F.A., Discrete Element Method for Modeling Solid and Particulate Materials, Ph.D. Thesis, Department of Engineering Physics, University of Wisconsin - Madison, 2005.
- Tavarez, F.A., and Plesha, M.E., Discrete Element Method for Modeling Solid and Particulate Materials, *Int'l. Journal for Numerical Methods in Engineering*, submitted for publication, 2006.
- Tavarez, F.A., and Plesha, M.E., Discrete Element Method for Modeling Damage and Penetration, in progress.